

# Advanced Nanoparticle Coatings for Stabilizing Layered Ni-Rich Oxide Cathodes in Solid-State Batteries

Yuan Ma,\* Jun Hao Teo, Felix Walther, Yanjiao Ma, Ruizhuo Zhang, Andrey Mazilkin, Yushu Tang, Damian Goonetilleke, Jürgen Janek,\* Matteo Bianchini, and Torsten Brezesinski\*

Improving the interfacial stability between cathode active material (CAM) and solid electrolyte (SE) is a vital step toward the development of high-performance solid-state batteries (SSBs). One of the challenges plaguing this field is an economical and scalable approach to fabricate high-quality protective coatings on the CAM particles. A new wet-coating strategy based on preformed nanoparticles is presented herein. Nonagglomerated nanoparticles of the coating material ( $\leq 5$  nm, exemplified for  $\text{ZrO}_2$ ) are prepared by solvothermal synthesis, and after surface functionalization, applied to a layered Ni-rich oxide CAM,  $\text{LiNi}_{0.85}\text{Co}_{0.10}\text{Mn}_{0.05}\text{O}_2$  (NCM85), producing a uniform surface layer with a unique structure. Remarkably, when used in pelletized SSBs with argyrodite  $\text{Li}_6\text{PS}_5\text{Cl}$  as SE, the coated NCM85 is found to exhibit superior lithium-storage properties ( $q_{\text{dis}} \approx 204$  mAh  $\text{g}_{\text{NCM85}}^{-1}$  at 0.1 C rate and 45 °C) and good rate capability. The key to the observed improvement lies in the homogeneity of coating, suppressing interfacial side reactions while simultaneously limiting gas evolution during operation. Moreover, this strategy is proven to have a similar effect in liquid electrolyte-based Li-ion batteries and can potentially be used for the application of other, even more favorable, nanoparticle coatings.

SEs have a mechanically rigid nature and a higher Li transference number ( $t_{\text{Li}^+} \approx 1$  vs  $t_{\text{Li}^+} \approx 0.5$  for liquid electrolytes), both being favorable for suppressing dendrite formation and facilitating the use of lithium-metal anodes.<sup>[1,3,4,6]</sup> In addition, SSBs have other advantages, such as a wider operation temperature range or no cross-talk effects due to electrode dissolution.<sup>[7,8]</sup>


Despite all that, commercialization of SSBs is hindered by their limited cycling performance compared to LIBs.<sup>[2,7,9]</sup> Especially ensuring compatibility of the cathode active material (CAM) with the SE and stability of their interface have proven difficult, as also the formation of cathode composites with proper ionic/electronic partial conductivities.<sup>[10]</sup> Thus, an important step toward the development of high-performance SSBs is the fabrication of a robust cathode.<sup>[9,11]</sup> Until now, different classes of superionic SEs (e.g., thiophosphates, oxides, polymers) have been proposed and studied for use in SSBs.<sup>[11,12]</sup> Lithium

thiophosphate-based SEs stand out due to soft mechanical properties (low elastic modulus), ensuring intimate particle/particle contact even by cold-pressing processes.<sup>[2,3,9]</sup> More importantly, this class of SEs presents Li-ion conductivities on the same order of magnitude as organic liquid electrolytes (e.g., for  $\text{Li}_6\text{PS}_5\text{Cl}$ ,  $\sigma_{\text{ion}}$  varies from  $\approx 3$  mS  $\text{cm}^{-1}$  at room temperature to 7 mS  $\text{cm}^{-1}$  at 45 °C, see related discussion in Figure S1, Supporting Information), allowing for satisfactory rate capability.<sup>[2,12,13]</sup> Regarding the CAM, layered Ni-rich NCMs ( $\text{LiNi}_{1-x-y}\text{Co}_x\text{Mn}_y\text{O}_2$ ), such

## 1. Introduction

The solid-state battery (SSB) is widely regarded as one of the most promising next-generation energy-storage technologies.<sup>[1–3]</sup> If successfully implemented, SSBs can have several advantages over conventional organic electrolyte-based Li-ion batteries (LIBs). For example, using superionic solid electrolytes (SEs), the environmental and safety issues posed by liquid electrolytes are dismissed in SSB systems.<sup>[2,4,5]</sup> Apart from that, inorganic

Y. Ma, J. H. Teo, R. Zhang, A. Mazilkin, D. Goonetilleke, J. Janek, M. Bianchini, T. Brezesinski  
Battery and Electrochemistry Laboratory  
Institute of Nanotechnology  
Karlsruhe Institute of Technology (KIT)  
Hermann-von-Helmholtz-Platz 1, 76344 Eggenstein-Leopoldshafen,  
Germany  
E-mail: yuan.ma@kit.edu; torsten.brezesinski@kit.edu

 The ORCID identification number(s) for the author(s) of this article can be found under <https://doi.org/10.1002/adfm.202111829>.

© 2022 The Authors. Advanced Functional Materials published by Wiley-VCH GmbH. This is an open access article under the terms of the Creative Commons Attribution License, which permits use, distribution and reproduction in any medium, provided the original work is properly cited.

DOI: 10.1002/adfm.202111829

F. Walther, J. Janek  
Institute of Physical Chemistry & Center for Materials Research  
Justus-Liebig-University Giessen  
Heinrich-Buff-Ring 17, 35392 Giessen, Germany  
E-mail: Juergen.Janek@phys.Chemie.uni-giessen.de

Y. J. Ma, Y. Tang  
Institute of Nanotechnology  
Karlsruhe Institute of Technology (KIT)  
Hermann-von-Helmholtz-Platz 1, 76344 Eggenstein-Leopoldshafen,  
Germany

A. Mazilkin  
Institute of Solid State Physics  
Russian Academy of Sciences  
Ac. Ossipyan str. 2, Chernogolovka 142432, Russia

M. Bianchini  
BASF SE  
Carl-Bosch-Str. 38, 67056 Ludwigshafen, Germany

as  $\text{LiNi}_{0.8}\text{Co}_{0.1}\text{Mn}_{0.1}\text{O}_2$  (NCM811) or  $\text{LiNi}_{0.85}\text{Co}_{0.10}\text{Mn}_{0.05}\text{O}_2$  (NCM851005, referred to as NCM85 for brevity), have great academic and industrial significance in advanced LIBs because of their high specific capacity ( $\geq 200 \text{ mAh g}^{-1}$ ) and high mean voltage ( $\geq 3.7 \text{ V vs Li}^+/\text{Li}$ ). For the same reasons, these CAMs are also considered state of the art for SSB applications.<sup>[14–16]</sup> Unfortunately, thiophosphate SEs have a relatively narrow electrochemical stability window (see also cyclic voltammetry (CV) data in Figure S1, Supporting Information) and show poor compatibility with NCM materials, in particular at high states of charge.<sup>[2,9,13,17]</sup> This in turn means that the cathode typically suffers from performance degradation during electrochemical cycling because of side reactions occurring at the interfaces, e.g., SE oxidation, leading to poor reversibility and resistance build-up.<sup>[2,9,13,18]</sup>

Applying a protective coating to the CAM surface is an effective strategy to improve the interfacial stability by avoiding direct physical contact with the SE.<sup>[2,9,17,19,20]</sup> An ideal coating should not only be thin and uniform, but also feature desirable properties, such as low electronic conductivity and high ionic conductivity. Such a coating would reduce the contact resistance caused by decomposition reactions, thereby enhancing the cycling performance.<sup>[2,9,20]</sup> To date, the most common methods are wet-chemical and dry coating, mainly for cost and processing reasons.<sup>[9,21]</sup> However, using these routes, both the thickness and morphology of the coating are difficult to control, leading to inhomogeneities and leaving areas of the surface unprotected.<sup>[9,21]</sup> Although some progress has been made in solving the aforementioned issues via atomic layer deposition, the high cost of precursors, poor scalability, and process complication limit its practical/commercial application.<sup>[21–24]</sup>

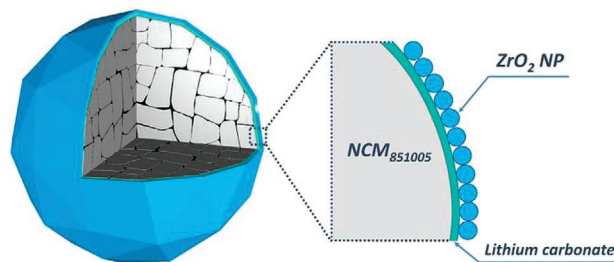
These challenges prompted the motivation for the present work, namely, developing a scalable coating method for fabricating a uniform, nanoscale layer on the NCM particle surface.<sup>[9,15,21]</sup> Specifically, we propose a new coating strategy based on preformed, nonagglomerated nanoparticles (NPs) in solution. Despite previous efforts to investigate and improve NP-derived coatings, the problem of inhomogeneities caused by large particle sizes and/or agglomeration remains to be solved.<sup>[25–27]</sup> Herein, the coating material was prepared first as a stable dispersion comprising monodisperse NPs ( $\leq 5 \text{ nm}$  size) and then applied to the CAM.  $\text{ZrO}_2$  NP-modified NCM85 served as a model system to demonstrate the effectiveness of the coating strategy. The as-formed material, referred to as  $\text{ZrO}_2$ -NCM85 hereafter, was characterized in pelletized (high-loading) SSB cells with  $\text{Li}_6\text{PS}_5\text{Cl}$  (see Figure S1, Supporting Information, for related material characteristics) and  $\text{Li}_4\text{Ti}_5\text{O}_{12}$

(LTO) as SE and anode, respectively.  $\text{ZrO}_2$  was selected because it has been reported in the past to be a robust coating material, owing to good chemical and electrochemical stability.<sup>[9,21,28,29]</sup> The results of this study not only highlight the formation of a  $\text{ZrO}_2$  monolayer coating with a constant thickness, but also with a unique bilayer structure (Scheme 1). It substantially enhanced the electrochemical performance of bulk-type SSB cells, delivering high reversible capacities and showing good cycling stability and rate capability (up to  $1140 \text{ mA g}_{\text{NCM85}}^{-1}$ ). The improvements can be attributed to changes in the CAM/SE interfacial stability, as demonstrated through a combination of operando and ex situ investigations. Data from complementary experiments are also presented (cycling performance of  $\text{ZrO}_2$ -NCM85 in LIBs and employing a different coating material,  $\text{HfO}_2$  NPs, having high (electro-)chemical stability, as reported elsewhere<sup>[24]</sup>), further emphasizing the versatility and potential of the new coating approach.

## 2. Results and Discussion

The coating procedure consists of two main steps: i) the preparation of a high-quality  $\text{ZrO}_2$  NP dispersion, and ii) its application to achieve a protective layer on the outer surface of the NCM85 particles. More details are provided in the Experimental Section. Note that both the coating content and the annealing temperature were optimized based on a series of control experiments. In summary, for the first step (fabrication of monodisperse  $\text{ZrO}_2$  NPs), we used a surfactant-free, nonaqueous solvothermal method (in benzyl alcohol).<sup>[30–32]</sup> Importantly, the as-prepared NPs showed high compositional homogeneity and purity,<sup>[31]</sup> as confirmed by powder X-ray diffraction (XRD, see Figure S2, Supporting Information). The XRD data revealed broad reflections as a result of the nanocrystalline nature of the  $\text{ZrO}_2$  particles.<sup>[33]</sup> The position and relative intensity of all reflections match well with those of the cubic crystal structure of zirconia. However, a turbid suspension was obtained after solvothermal reaction (Figure S3a, Supporting Information), indicative of NP agglomeration (high surface energy).<sup>[33,34]</sup> No apparent improvement was achieved upon redispersing the NPs in nonpolar or polar solvents.<sup>[30]</sup> Obviously, it would be difficult to produce a uniform coating on the NCM85 CAM using such aggregated NPs as the coating material (Figure S4, Supporting Information). Thus, a surface functionalization step was required to properly disperse the  $\text{ZrO}_2$  NPs. Specifically, minute quantities of long-chain ligands (oleic acid in this case) were added to the suspension to offer stabilization in nonpolar solvents (chloroform) via steric hindrance.<sup>[30,32,33]</sup> Ultimately, a highly stable and transparent dispersion of  $\text{ZrO}_2$  NPs was obtained, as shown in Figure S3b of the Supporting Information, coupled with a high solid content of up to  $70 \text{ mg mL}^{-1}$ . Transmission electron microscopy (TEM) imaging showed evenly dispersed NPs with a narrow size distribution of 3–5 nm (Figure S3c–e, Supporting Information). The lattice spacing of 0.18 nm, recorded in high-resolution TEM (HRTEM, see Figure S3d, Supporting Information), is identical with the distance of the (220) lattice planes of cubic  $\text{ZrO}_2$ .

After application of the coating, the  $\text{ZrO}_2$ -NCM85 CAM was characterized via XRD, X-ray photoelectron spectroscopy (XPS), and scanning electron microscopy (SEM) in an attempt to probe



**Scheme 1.** Schematic coating morphology. The protective coating has a unique bilayer structure, consisting of  $\text{ZrO}_2$  NPs and (mostly) lithium carbonate.

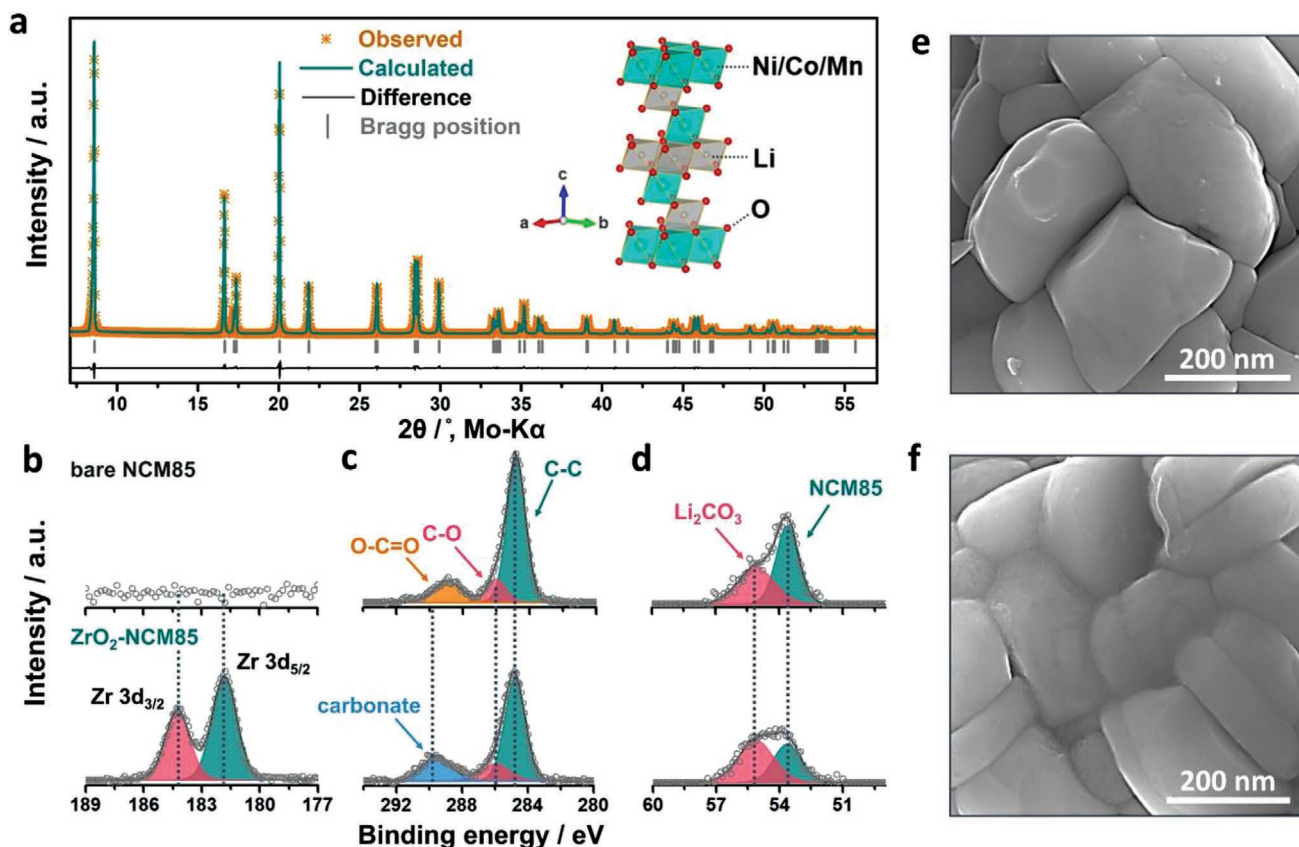


**Figure 1.** Structural and (near) surface characteristics of the  $\text{ZrO}_2\text{-NCM85}$ . a) Powder XRD pattern and corresponding Rietveld refinement plot. Observed, calculated, and difference profiles are shown in orange, cyan, and black, respectively. Markers (gray) indicate the expected Bragg reflections for NCM85, and the inset displays the crystal structure model. The fitting results are given in Table S1 of the Supporting Information. XPS detail spectra of the b) Zr 3d, c) C 1s, and d) Li 1s core levels for the bare NCM85 (top) and  $\text{ZrO}_2\text{-NCM85}$  (bottom). Note that the C 1s and Li 1s spectra have the same y-axis scaling for the different materials. SEM images of the e) bare NCM85 and f)  $\text{ZrO}_2\text{-NCM85}$ .

the crystal structure and surface chemistry. XRD (Figure 1a) showed that the  $\text{ZrO}_2\text{-NCM85}$  has the expected O3-type layered structure ( $R\text{-}3m$  space group, see also crystal structure model in the inset of Figure 1a). Refinement of structural models against the diffraction data revealed that the lattice parameters of the coated CAM remain constant within error, see Figure S5 and Table S1 of the Supporting Information, while no appreciable impact on the Ni/Li cation mixing was observed either, 2.9(2)% for bare NCM85 and 3.4(3)% for  $\text{ZrO}_2\text{-NCM85}$ . This indicates that the coating process at least does not significantly affect the structural properties of the NCM85 CAM (Figure S6, Supporting Information).<sup>[15]</sup> The absence of unforeseen reflections further highlights the purity of the material. Reflections from the  $\text{ZrO}_2$  NPs were not found in the XRD pattern (see Figure 1a; Figure S6, Supporting Information), which is expected due to low overall crystallinity and content. Inductively coupled plasma-optical emission spectroscopy (ICP-OES, see Table S2, Supporting Information) revealed a Zr content of 0.66 wt%, equivalent to 0.92 wt%  $\text{ZrO}_2$ .

The XPS detail spectra of the Zr 3d, C 1s, and Li 1s regions in Figure 1b–d contain compositional information about the coating. Figure 1b shows two Zr 3d signals, Zr 3d<sub>5/2</sub> at 181.9 eV and Zr 3d<sub>3/2</sub> at 184.2 eV,<sup>[35,36]</sup> confirming the presence of a  $\text{ZrO}_2$  coating, in agreement with the ICP-OES results. As expected, the Zr 3d signals were absent for the bare NCM85 CAM. The

$\text{ZrO}_2\text{-NCM85}$  had a more pronounced C 1s contribution than the bare NCM85 at 289.6 eV (Figure 1c), which was not the case for the other three peaks (284.8 eV for C=C/C–C, 286.0 eV for C–O, and 288.9 eV for O=C–O).<sup>[37–39]</sup> The binding energy of the increased signal contribution is in the typical range of carbonate species, such as  $\text{Li}_2\text{CO}_3$ ,<sup>[37,38]</sup> which most likely stem from the ligand and/or solvent decomposition during the final heating step at 400 °C. The presence of  $\text{Li}_2\text{CO}_3$  (main surface carbonate) was further corroborated by the fact that the corresponding contribution in the Li 1s core-level region remained virtually unaltered after coating (Figure 1d), while the NCM85 signal intensity strongly decreased.<sup>[37,38]</sup> These findings suggest that the carbonate fraction is part of the coating in the  $\text{ZrO}_2\text{-NCM85}$  CAM.<sup>[18]</sup> Additionally, attenuated total reflection-infrared (ATR-IR) spectroscopy confirmed the presence of surface carbonate species (Figure S7, Supporting Information).

Surface characterization of the CAM in the pristine state and after coating was done by SEM (Figure 1e,f; Figure S8, Supporting Information). Low-magnification SEM imaging (Figure S8, Supporting Information) indicated that both the  $\text{ZrO}_2\text{-NCM85}$  and bare NCM85 CAMs possess a uniform (polycrystalline) morphology with an average secondary particle size of 3  $\mu\text{m}$ . This confirms that the NCM85 retains its original structure/morphology upon coating. As can be seen from the high-magnification SEM image in Figure 1e, the top surface of

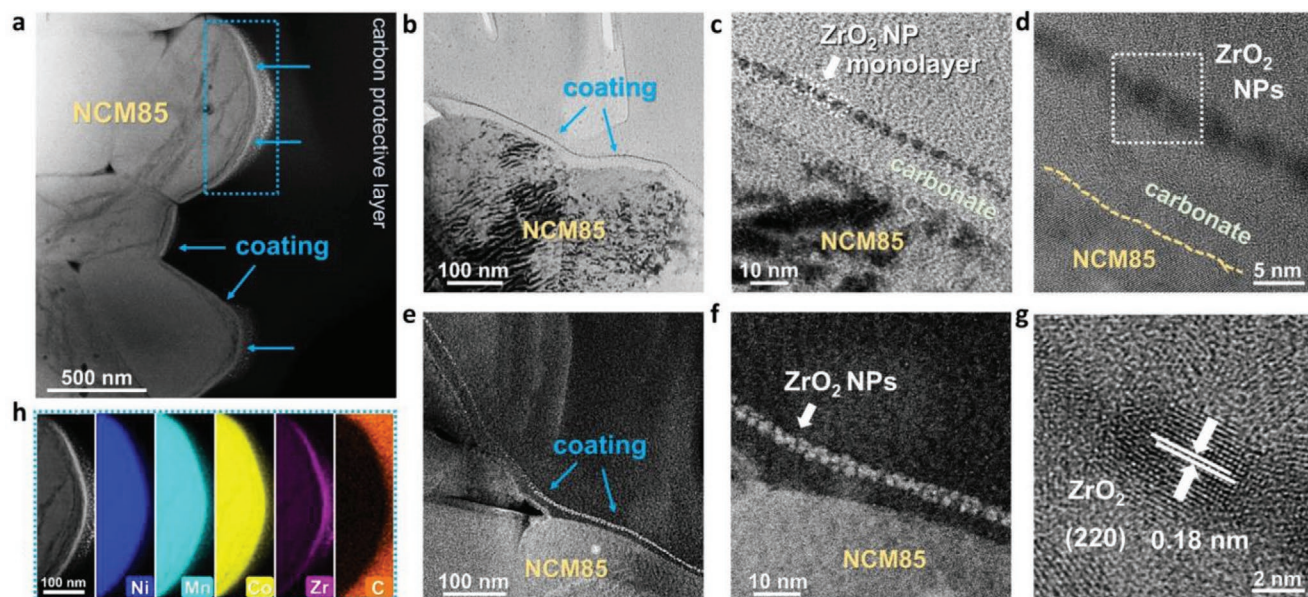


**Figure 2.** Coating structure of the  $\text{ZrO}_2$ -NCM85. a,e,f) Low- and high-magnification HAADF STEM images. b–d) TEM images at different magnifications. g) HRTEM image of the area indicated in (d). h) EDS mapping of the area denoted by the dashed box in (a).

the bare NCM85 primary particles appeared quite smooth. Similarly, the  $\text{ZrO}_2$ -NCM85 particles also had a relatively smooth surface (Figure 1f), probably owing to uniform NP deposition.

To gain more insight into the coating microstructure, (scanning) TEM [(S)TEM] and energy-dispersive X-ray spectroscopy (EDS) mapping were conducted on focused-ion beam (FIB)-prepared specimens, as summarized in Figure 2. Note that a carbon layer was deposited onto the  $\text{ZrO}_2$ -NCM85 CAM to protect the coating from damage during sample preparation and processing. Low-magnification high-angle annular dark-field (HAADF) STEM imaging (Figure 2a) showed that the free surface of the NCM85 secondary particles is uniformly covered by a shell-like structure. Interestingly, the TEM image in Figure 2b reveals a dual coating structure, consisting of an outer darker layer and an inner lighter layer. The outer layer is a monolayer, stemming from the organized assembly of  $\text{ZrO}_2$  NPs, see TEM images in Figure 2c,d. The inner layer has a quasi amorphous nature and is represented in a lighter contrast. The monolayer exhibits a thickness of 4–5 nm, which agrees well with the size of the  $\text{ZrO}_2$  NPs (Figure S3c–e, Supporting Information). The HRTEM image in Figure 2g shows the lattice fringes of the NPs with a  $d$ -spacing of 0.18 nm for the (220) planes. Notably, Figure 2d also shows  $\text{ZrO}_2$  lattice fringes within the inner layer (see also Figure S9, Supporting Information). This may be because i) some NPs are not involved in the formation of the protective shell and/or ii) FIB milling causes material damage, leading to partial exfoliation of NPs from the outer monolayer. Moreover, from the high-magnification HAADF STEM images (see Figure 2e,f, showing different NCM85 surfaces), it can be seen that the inner layer exhibits a similar contrast to the deposited protective carbon layer. These results combined with the XPS and ATR-IR spectroscopy data suggest that carbonate, probably  $\text{Li}_2\text{CO}_3$ , is the second main component of the  $\text{ZrO}_2$ -based coating.<sup>[40,41]</sup> This is further confirmed by electron energy-loss spectroscopy (EELS) mapping of the  $\text{ZrO}_2$ -NCM85 surface (Figure S10, Supporting Information).

The thickness of the inner layer (Figure 2b,c,e), which seems to be derived from the decomposition of the oleic acid ligands used for functionalization of the NPs, is relatively constant along the coating ( $\approx 8$  nm). By contrast, when using a solution that contained only oleic acid and no  $\text{ZrO}_2$  NPs for coating the NCM85 CAM (referred to as C-NCM85, related characterization data presented in Figures S11–S15, Supporting Information), HAADF STEM imaging revealed the presence of irregular deposits on the particle surface.<sup>[40]</sup> The lack of a continuous carbonaceous layer, as compared to the  $\text{ZrO}_2$ -NCM85 sample, demonstrates that the NPs play a critical role in the fabrication of a high-quality coating with uniform thickness and good surface coverage. More experiments will be performed in the future to unveil the details of the formation mechanism and the role of the main components.

Finally, the conclusions drawn from (S)TEM imaging were validated by EDS elemental mapping (Figure 2h), verifying that the  $\text{ZrO}_2$  NPs primarily distribute on the outer surface (light shell) of the NCM85 secondary particles. Note that the resolution is not high enough to distinguish the carbonaceous coating from the protective carbon layer (see EELS mapping results in Figure S10, Supporting Information, instead).

The electrochemical performance of the uncoated (bare NCM85), coated ( $\text{ZrO}_2$ -NCM85), and reference (C-NCM85) CAMs was investigated in pelletized SSB cells with a high areal loading [ $(11.0 \pm 0.3) \text{ mg}_{\text{NCM85}} \text{ cm}^{-2}$ ,  $\approx 2.1 \text{ mAh cm}^{-2}$ ]. The cathode composite consisted of the respective CAM, SE ( $\text{Li}_6\text{PS}_5\text{Cl}$ ), and carbon additive (Super C65).  $\text{Li}_6\text{PS}_5\text{Cl}$  SE was also used in the separator layer, and a composite comprising LTO,  $\text{Li}_6\text{PS}_5\text{Cl}$ , and Super C65 served as anode. All cells were galvanostatically cycled at 45 °C and at various C-rates in a voltage range of 1.35–2.75 V versus  $\text{Li}_4\text{Ti}_5\text{O}_{12}/\text{Li}_7\text{Ti}_5\text{O}_{12}$ , corresponding to  $\approx 2.9$ –4.3 V versus  $\text{Li}^+/\text{Li}$ . Figure 3a shows the voltage–capacity profiles of the first 2 cycles at 0.1 C rate. The different electrochemical performance indicators for the initial cycle are displayed in the form of a radar plot in

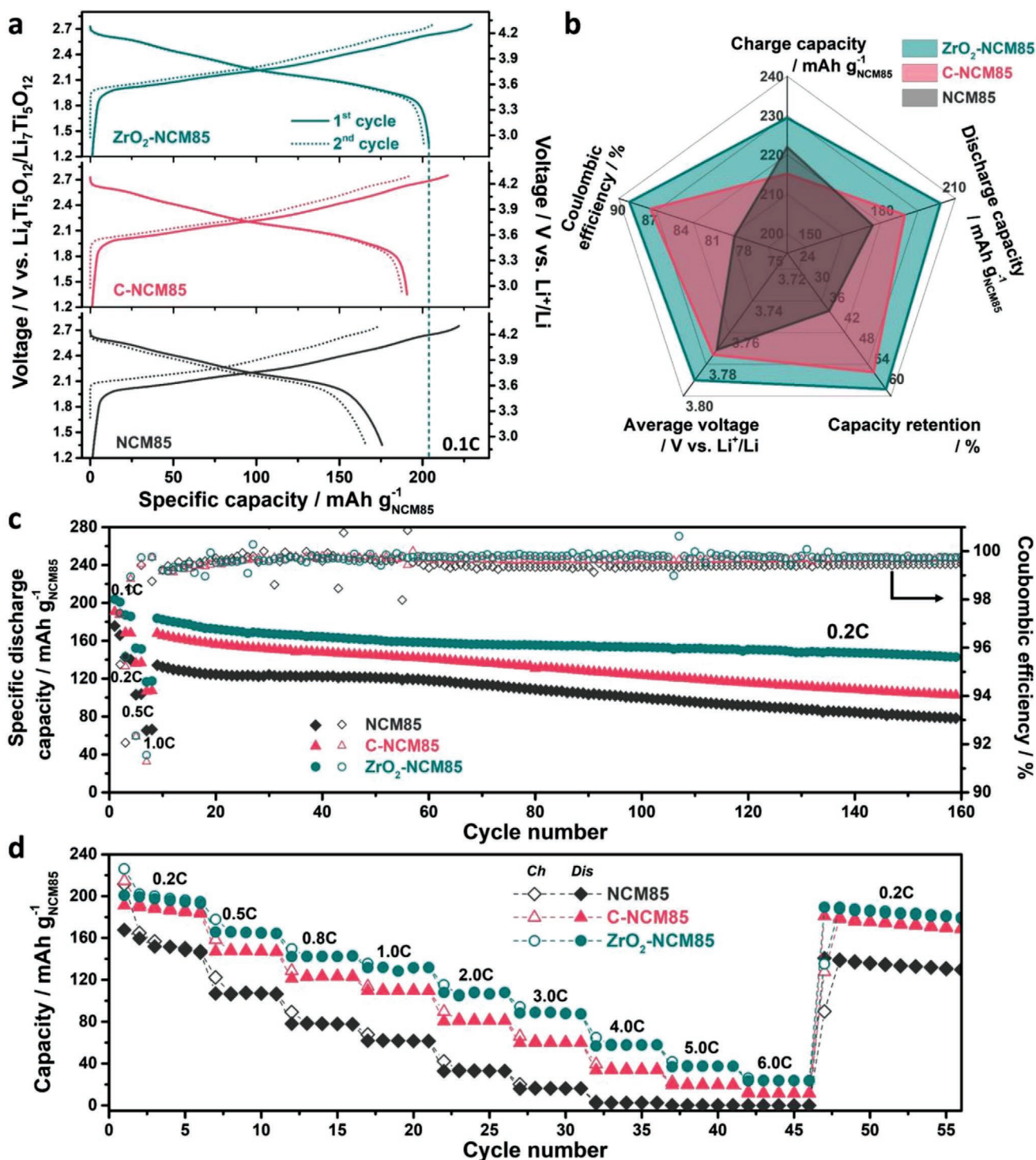


**Figure 3.** Cycling performance of the bare NCM85, C-NCM85, and ZrO<sub>2</sub>-NCM85 in SSB cells at 45 °C. a) First- and second-cycle voltage profiles at a rate of 0.1 C. b) First-cycle performance indicators and capacity retention calculated by dividing the discharge capacity at 1.0 C by the initial discharge capacity at 0.1 C. c) Rate and long-term cycling performance tests. The C-rate was varied from 0.1 C to 1.0 C over the initial 8 cycles, followed by cycling at 0.2 C. d) Specific (dis-)charge capacities at different C-rates versus the cycle number.

Figure 3b. In the initial cycle, the bare NCM85 delivered specific charge and discharge capacities of 221 and 175  $\text{mAh g}^{-1}_{\text{NCM85}}$ , respectively, corresponding to a Coulombic efficiency of 79%. For the C-NCM85, the capacities amounted to 217 and

190  $\text{mAh g}^{-1}_{\text{NCM85}}$ , thus indicating a lower irreversible capacity loss (87% Coulombic efficiency). The largest specific capacities of 229  $\text{mAh g}^{-1}_{\text{NCM85}}$  (charge) and 204  $\text{mAh g}^{-1}_{\text{NCM85}}$  (discharge) and the highest Coulombic efficiency of 89% were

obtained with the ZrO<sub>2</sub>-NCM85 CAM, which can be attributed to the good surface coverage and uniformity of the protective coating.<sup>[2,9,41]</sup> The beneficial effect of the NP coating is further evident from the comparison of the first-cycle discharge curves (Figure S16, Supporting Information), revealing substantial improvements in voltage drop and a higher mean voltage (Figure 3b) for the ZrO<sub>2</sub>-NCM85, compared to the C-NCM85 and bare NCM85 CAMs. This result suggests that the coating is capable of suppressing side reactions, thereby reducing the interfacial impedance and polarization, as also apparent from the differential capacity curves and CV profiles in Figures S17 and S18 of the Supporting Information.

In the second cycle, virtually no capacity fading was observed for the ZrO<sub>2</sub>-NCM85 and C-NCM85, confirming good reversibility.<sup>[39]</sup> By contrast, the specific discharge capacity of the bare NCM85 cell decayed to 165 mAh g<sub>NCM85</sub><sup>-1</sup>, accompanied by an increase in overpotential, indicating that irreversible processes continued to occur after the initial cycle. The long-term performance measurements in Figure 3c included rate capability testing from 0.1 C/0.1 C to 1.0 C/1.0 C (2 cycles at each C-rate), followed by cycling at a constant charge/discharge rate of 0.2 C. The ZrO<sub>2</sub>-NCM85 CAM clearly exhibited better rate performance than the other two samples. In particular, the retention at 1.0 C maintained at a high value of ≈60% with respect to the first-cycle discharge capacity at 0.1 C (Figure 3b), compared to only 37% and 55% for the bare NCM85 and C-NCM85, respectively. The reversible Li-storage capacity of the ZrO<sub>2</sub>-NCM85 CAM in SSBs was also significantly improved, with  $q_{\text{dis}} \approx 156 \text{ mAh g}_{\text{NCM85}}^{-1}$  after 160 cycles, corresponding to 83% retention relative to the cell capacity in the 9th cycle. By contrast, the C-NCM85- and bare NCM85-based SSBs showed significant capacity degradation upon cycling, delivering specific discharge capacities of 101 and 68 mAh g<sub>NCM85</sub><sup>-1</sup>, respectively, after 160 cycles (60% and 55% capacity retention). We note that preliminary data indicate that the LTO anode is stable and has no major effect on the performance of the NCM85 CAMs. As for the Coulombic efficiency, Figure 3c reveals a rapid increase after the initial cycle for all cells, finally stabilizing above 99% from the 20th cycle onward. Among them, the ZrO<sub>2</sub>-NCM85 showed a higher Coulombic efficiency (up to 99.8%) after 50 cycles, suggesting improved CAM/SE interfacial stability.

The SSB cells were also subject to a wider range of galvanostatic charge/discharge rates from 0.2 to 6.0 C, as shown in Figure 3d and Figure S19 (Supporting Information). A good rate capability was achieved when using the ZrO<sub>2</sub>-NCM85 CAM, delivering stable specific capacities of 197, 166, 143, 132, 107, and 89 mAh g<sub>NCM85</sub><sup>-1</sup> at 0.2 C, 0.5 C, 0.8 C, 1.0 C, 2.0 C, and 3.0 C, respectively. At even higher C-rates of 4.0 C, 5.0 C, and 6.0 C, it was still capable of delivering 58, 38, and 25 mAh g<sub>NCM85</sub><sup>-1</sup>, respectively. Notably, a specific capacity of 190 mAh g<sub>NCM85</sub><sup>-1</sup> was recovered at 0.2 C after the rate performance testing in the 48th cycle, further emphasizing the stability of this material. By comparison, the C-NCM85 CAM delivered inferior specific capacities at all C-rates (e.g., 59 and 19 mAh g<sub>NCM85</sub><sup>-1</sup> at 3.0 C and 5.0 C, respectively). The bare NCM85 exhibited the worst electrochemical performance among the three CAMs and showed a substantially lower rate capability, with an obvious capacity fading during the first cycles at 0.2 C. At C-rates ≥ 4.0 C, the specific capacity was reduced to virtually zero mAh g<sub>NCM85</sub><sup>-1</sup>. This poor rate performance can be attributed

to a strongly increasing overpotential with increasing C-rate (see voltage profiles in Figure S19, Supporting Information).<sup>[42]</sup> The increase was largest for the bare NCM85, followed by C-NCM85 and ZrO<sub>2</sub>-NCM85. Especially for SSB cells using the latter material, variation of the internal resistance was moderate, leading to fast kinetics and good cycling stability. Considering the poor conductivity of ZrO<sub>2</sub>, the charge transport across the CAM/SE interface should be hampered with coating. However, the results from rate capability experiments suggest that interfacial side reactions play a more significant role in the performance degradation.

Overall, the improvements achieved are due to i) the high surface coverage, preventing interfacial side reactions from occurring, and more importantly, ii) the uniform distribution of ZrO<sub>2</sub> NPs in the coating, avoiding sluggish transfer kinetics typically caused by thick coatings.<sup>[2,9]</sup> The performance improvements were also confirmed by galvanostatic intermittent titration technique (GITT) measurements (Figure S20, Supporting Information), indicating decreasing polarization in the order of ZrO<sub>2</sub>-NCM85 > C-NCM85 > bare NCM85.

Another factor contributing to performance degradation, especially capacity fading during cycling, is the inherent interfacial instability.<sup>[2]</sup> To achieve a better understanding of this effect, ex situ electrochemical impedance spectroscopy (EIS) measurements were conducted at 45 °C on the different SSB cells after 50 and 160 cycles. The results are shown in Figure 4a–d and Table S3 (Supporting Information). The Nyquist plots of the electrochemical impedance showed a depressed semicircle and a single line in the high- and low-frequency range, respectively. The fitting results (see equivalent circuit model in the inset of Figure 4a) indicate that the cells have a similar bulk resistance ( $R_{\text{Bulk}}$ ) ranging from 21 to 30 Ω, which is typically considered as the SE resistance.<sup>[41,43,44]</sup> The SE grain boundary resistance ( $R_{\text{GB}}$ ) was found to be 13–26 Ω. The slight variations are believed to originate from local electrode inhomogeneities.<sup>[41]</sup> The CAM/SE interfacial resistance ( $R_{\text{CAM/SE}}$ ) contributed the most to the difference in cell impedance among the three samples. At the 50th cycle, the  $R_{\text{CAM/SE}}$  followed the order of bare-NCM85 (437 Ω) > C-NCM85 (125 Ω) > ZrO<sub>2</sub>-NCM85 (36 Ω). The  $R_{\text{CAM/SE}}$  increased by a factor of about two after 160 cycles. In contrast to the bare-NCM85 (893 Ω), the  $R_{\text{CAM/SE}}$  of the ZrO<sub>2</sub>-NCM85-based cell (82 Ω) was an order of magnitude lower. These findings are in line with the trends observed from the electrochemical testing and further corroborate the effectiveness of the double-layer coating in suppressing the formation of detrimental SE degradation products.

The decrease in side reactions with application of a protective coating is also evident from top-view SEM images obtained on the cathode composites using the uncoated and coated NCM85 CAMs before and after cycling. The NCM85 and Li<sub>6</sub>PS<sub>5</sub>Cl particles can be clearly distinguished from one another in the SEM image of the pristine cathode (Figure 4e). After 160 cycles, the cathode with the bare NCM85 revealed significant changes in surface and bulk morphology (Figure 4f). Specifically, the formation of a porous structure between the NCM85 secondary particles (in the previous SE regions) and the appearance of a thick layer on the CAM surface indicated SE decomposition upon cycling. For the C-NCM85, a similar evolution in SE appearance was observed (Figure 4g), albeit to a lesser degree. This kind of degradation was not visible for

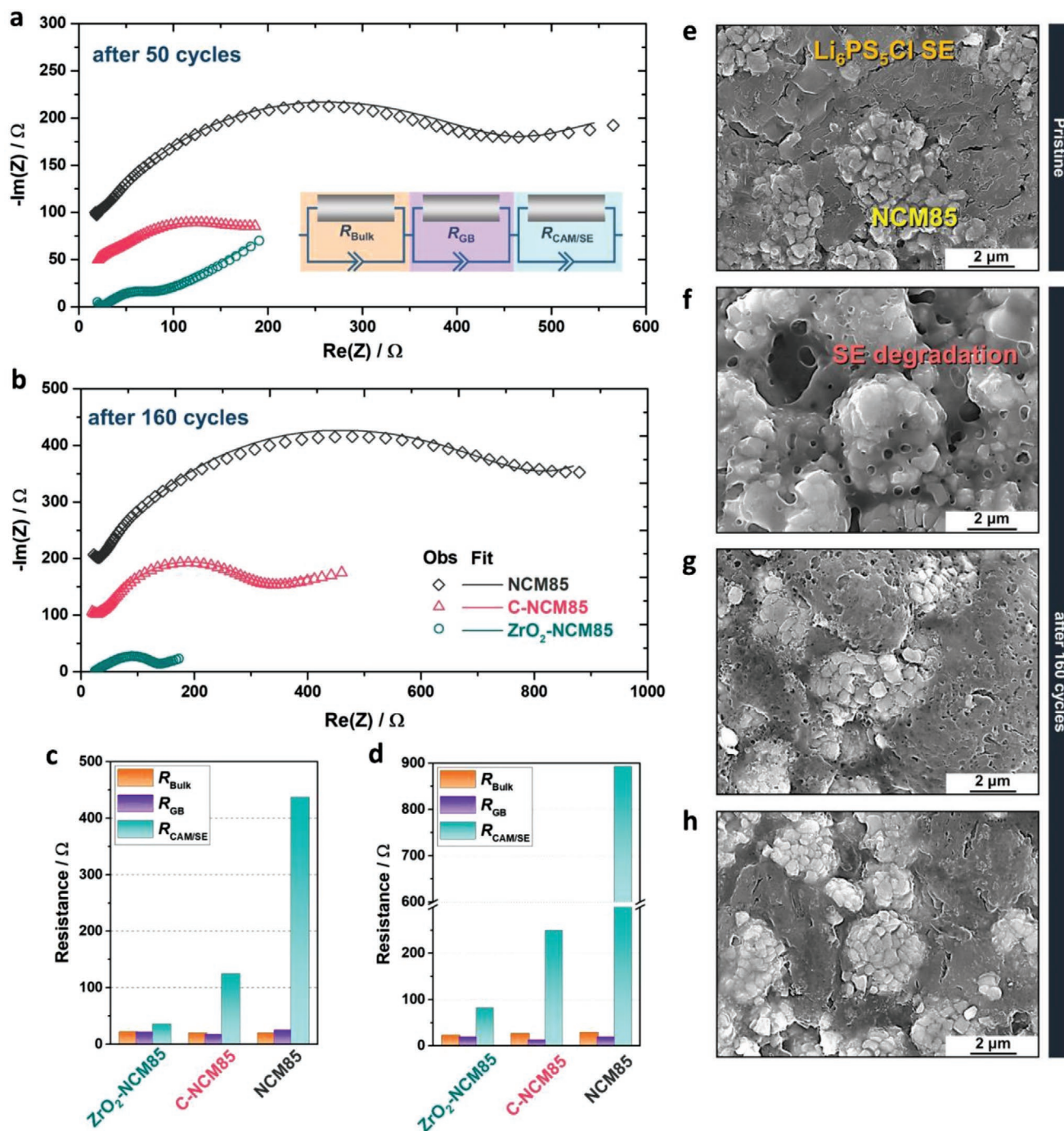


**Figure 4.** Nyquist plots of the electrochemical impedance for SSB cells using the bare NCM85 (black), C-NCM85 (red), and  $ZrO_2$ -NCM85 (cyan) after a) 50 and b) 160 cycles at a rate of 0.2 C and 45 °C in the discharged state. The inset in (a) shows the equivalent circuit used to fit the EIS data and describe the resistance contributions from the bulk SE ( $R_{Bulk}$ ), SE grain boundary ( $R_{GB}$ ), and CAM/SE interface ( $R_{CAM/SE}$ ). c, d) Summary of the fitting results. e–h) Top-view SEM images of the cathode (e) in the pristine state and (f–h) after 160 cycles:  $ZrO_2$ -NCM85 (e, h), bare NCM85 (f), and C-NCM85 (g).

the  $ZrO_2$ -NCM85-based cathode composite (Figure 4h). The original electrode structure was well maintained after cycling, indirectly stressing that the CAM/SE interface is reasonably robust in terms of stability. These results agree well with those from cross-sectional SEM imaging (Figure S21, Supporting Information). Interestingly, there were no apparent signs of cracking or damage (electrochemical contact loss) near the

CAM/SE interface. This suggests that (chemo-)mechanical degradation within the cathode does not play a critical role in the differences in cyclability between the bare and coated NCM85 CAMs in these cells.<sup>[8]</sup> Additionally, XRD data collected from the cathode composites in the pristine state and after cycling showed that the bulk structure of  $Li_6PS_5Cl$  remains stable (see Figure S22 and Table S4, Supporting Information).

The differences in the  $R_{CAM/SE}$  and the electrode morphology/microstructure between the cathode composites are largely attributed to the chemistry and thickness of the surface decomposition layer. To examine the chemical nature of the degradation products, ex situ XPS and time-of-flight secondary ion mass spectrometry (ToF-SIMS) measurements were performed after 50 cycles. Figure 5a shows XPS detail spectra of the S 2p and P 2p core-level regions for both the pristine  $\text{Li}_6\text{PS}_5\text{Cl}$  SE and the cycled cathodes. The S 2p spectrum of  $\text{Li}_6\text{PS}_5\text{Cl}$  consisted of four doublets. While the pronounced doublet at 161.7/162.9 eV is characteristic of the  $\text{PS}_4^{3-}$  units of the argyrodite structure, that at a lower binding energy (160.3/161.4 eV) represents  $\text{Li}_2\text{S}$  impurities (or “free”  $\text{S}^{2-}$  ions).<sup>[8,18,45]</sup> The other two minor doublets located at higher binding energies (162.9/164.1 and 163.7/164.9 eV) can be assigned to various compounds, including anionic frameworks that thiophosphate phases can pass through upon oxidative decomposition toward the formation of  $\text{P}_2\text{S}_5$  (e.g.,  $\text{P}_2\text{S}_7^{4-}$ ,  $\text{P}_2\text{S}_6^{2-}$ ) and “S<sup>0</sup>” species, such as long-chain polysulfides.<sup>[8,18]</sup> The P 2p spectrum showed two doublets at 132.0/132.8 and 133.0/133.9 eV, representing the  $\text{PS}_4^{3-}$  units and the aforementioned degradation products and/or lithium phosphate, respectively.<sup>[18,45–47]</sup> The presence of the latter may be a result of the reaction with trace water/oxygen because of the high reactivity of the  $\text{Li}_6\text{PS}_5\text{Cl}$  SE.<sup>[2,13,45]</sup> After 50 cycles, the peaks associated with the oxidized sulfur species in the S 2p data increased in intensity for all three cathodes, indicating the decomposition of the thiophosphate SE upon cycling. The coated CAMs showed slightly lower signals compared to the uncoated counterpart (Figure S23, Supporting Information). This confirms that the coatings are capable of partly suppressing the SE degradation. However, the formation of degradation products still seems pronounced and further differentiation between both coated samples is not possible. Note that several degradation zones (in the cathode) overlap in the XPS analysis area and therefore in the signals, as recently reported.<sup>[48]</sup> The oxidative SE decomposition can, in principle, occur at the CAM/SE and carbon additive/SE interfaces.<sup>[48,49]</sup> Because the carbon black used in this work was not modified/protected, degradation is believed to occur unhindered at this interface.<sup>[49]</sup> Consequently, the emerging signals in the S 2p data are expected to be dominated by SE decomposition processes at the carbon additive/SE interface, making a separation of the CAM/SE contribution virtually impossible.

By contrast, changes in the P 2p spectra allow for a better assignment of decomposition signals to the CAM/SE interface due to less interference. In particular, a new doublet at a higher binding energy (P  $2p_{3/2}$  at 134.5 eV) appeared upon cycling because of the formation of oxygenated phosphorus species (phosphates, metaphosphates, etc.).<sup>[18,45]</sup> Since the CAM is usually the only oxygen source in the cathode, the oxygenated phosphorus species can be directly correlated with the interfacial reaction between CAM and SE.<sup>[18]</sup> While the C-NCM85 already revealed a slight decrease in such by-products, the  $\text{ZrO}_2$ -NCM85-based cathode showed the lowest intensity of this P 2p doublet contribution and the lowest relative amount of degradation products in general (Figure S23, Supporting Information). This result provides evidence of suppressed side reactions at the CAM/SE interface as the working principle of

the protective coatings. However, the effect appears to be much stronger when using the  $\text{ZrO}_2$ -NCM85 CAM, which in turn helps explain the above findings.

To gain a better understanding of the interfacial processes occurring within the electrodes, ToF-SIMS analysis was performed on the different cathode composites (after 50 cycles). ToF-SIMS possesses a high sensitivity and therefore allows probing degradation phenomena and the effect of the CAM coating beyond the XPS detection limit. The results from surface analysis and depth profiling are depicted in Figure 5b,c, showing boxplots for the normalized intensity of the phosphate ( $\text{PO}_x^-$ ) and sulfate/sulfite ( $\text{SO}_x^-$ ) fragments. The formation of  $\text{PO}_x^-/\text{SO}_x^-$  species is a clear sign of degradation at the CAM/SE interface.<sup>[45,48,50]</sup> In the case of surface analysis (Figure 5b), both the bare NCM85 and C-NCM85 cathodes displayed similar intensities (slightly higher for the C-NCM85) for the  $\text{PO}_2^-/\text{PO}_3^-$  and  $\text{SO}_2^-$  fragments. Only the  $\text{SO}_3^-$  fragment showed a decrease in intensity for the C-NCM85 cathode, indicating less formation of oxygenated sulfur species. For the  $\text{ZrO}_2$ -NCM85 cathode, reduction in signal intensities for both the  $\text{PO}_x^-$  and  $\text{SO}_x^-$  fragments was clearly visible, demonstrating suppression of the oxygen-involving interfacial reactions between CAM and SE. The trend of the phosphate fragments in the surface analysis seems to contradict the XPS results, as the C-NCM85 cathode did not show decreased formation of oxygenated phosphorus species. However, it should be noted that the surface facing the current collector was probed. The analyzed region therefore contains convoluted information about all interfacial reactions (current collector/SE, carbon additive/SE, and CAM/SE) and is likely dominated by the current collector/SE contribution.<sup>[48,51]</sup> Ultimately, this can lead to measurement uncertainties because of strong mass interferences and variations in total ion intensity (and therefore variations in the normalization approach) among others.

To eliminate the influence of the current collector, depth profiling was done on near-surface regions of the cycled cathodes.<sup>[45]</sup> Figure 5c shows the results from these experiments. It can be seen that the trends in intensity for the  $\text{PO}_x^-$  and  $\text{SO}_x^-$  fragments match with the cycling performance, the impedance, and the trends observed in the P 2p spectra (Figures 3c, 4a, and 5a). The signals suggest decreasing oxygen-involving side reactions in the order of  $\text{ZrO}_2$ -NCM85 > C-NCM85 > bare NCM85.

In contrast to XPS, ToF-SIMS was able to show suppressed formation of oxygenated sulfur species by surface coating because of the higher sensitivity of the analytical method.<sup>[18,45,48]</sup> In addition, this facilitated the differentiation of both coatings regarding their effect on the interfacial reactions between CAM and SE.

ToF-SIMS measurements were also conducted on crater sidewalls, providing information about the local distribution of fragments with high lateral resolution.<sup>[18,45]</sup> The secondary ion images for the cathode using the  $\text{ZrO}_2$ -NCM85 are shown in Figure 5d. Each component in the composite could be well resolved by utilizing the respective (specific) fragments. The  $\text{ZrO}_2^-$  signal indicated that the NP coating maintains a high density (and uniformity) around the NCM85 secondary particles after cycling, thus suggesting that it is capable of addressing consumption issues caused by diffusion and/or



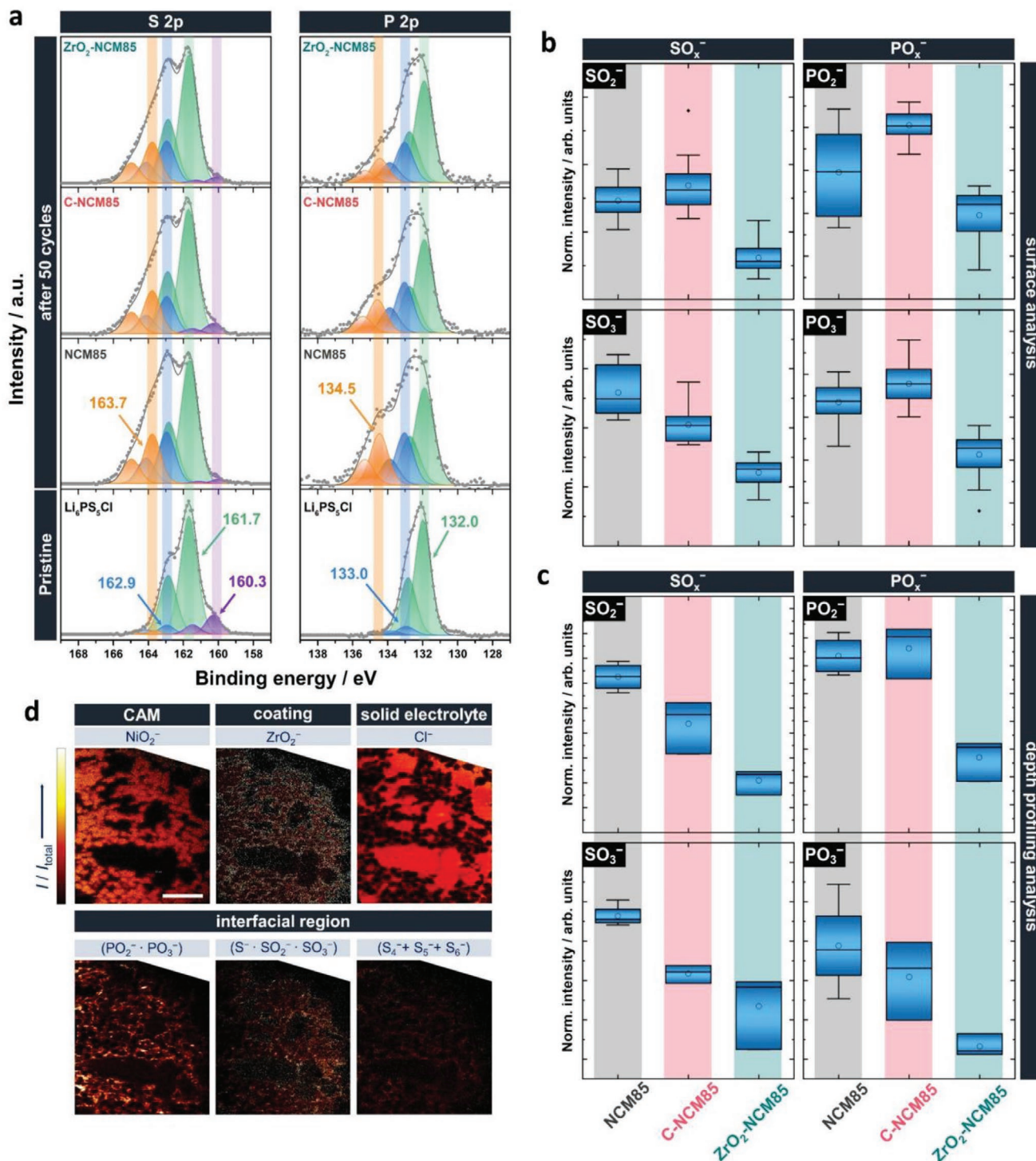


**Figure 5.** Characterization of the interfacial degradation after 50 cycles at a rate of 0.2 C and 45 °C. a) XPS detail spectra of the S 2p (left) and P 2p (right) core-level regions. The surface was previously cleaned by sputtering with Ar<sup>+</sup> ions to reduce detrimental effects of the current collector. Reference spectra for the pristine Li<sub>6</sub>PS<sub>5</sub>Cl SE are shown at the bottom (see Figure S23, Supporting Information, for comparison of relative amounts of the S 2p/P 2p components). b–d) Results from ToF-SIMS measurements. Boxplots of the normalized intensity of PO<sub>x</sub><sup>-</sup> and SO<sub>x</sub><sup>-</sup> fragments (with 2 ≤ x ≤ 3) from (b) surface analysis (≥14 measurements per sample) and (c) depth profiling (≥3 measurements per sample). Data were normalized to the total ion intensity. (d) Exemplary normalized secondary ion images of negatively charged fragments on an FIB crater sidewall (45°) of the cathode using the ZrO<sub>2</sub>-NCM85. The CAM (NiO<sub>2</sub><sup>-</sup>), the coating (ZrO<sub>2</sub><sup>-</sup>), the SE (Cl<sup>-</sup>), and the degradation products [(PO<sub>2</sub><sup>-</sup> · PO<sub>3</sub><sup>-</sup>), (S<sup>-</sup> · SO<sub>2</sub><sup>-</sup> · SO<sub>3</sub><sup>-</sup>), and polysulfides] can be clearly distinguished from one another.

(electro-)chemical reactions.<sup>[18]</sup> Moreover, secondary ion images of fragments that can be attributed to degradation products confirmed that side reactions occur in the bulk of the electrode irrespective of the coating. The signals mainly appeared at the CAM/SE interface and denote both oxidative SE decomposition (long-chain polysulfides ( $S_x^-$ )) and (electro-)chemical CAM/SE reactions (oxygenated phosphorus and sulfur species ( $PO_x^-$  and  $SO_x^-$ )). Similar fragment distributions were observed for composites with the bare NCM85 and C-NCM85 CAMs (Figure S24, Supporting Information). Overall, these results show that protective CAM coatings may indeed suppress unfavorable reactions at the interface with the SE, leading to significantly improved electrochemical performance in bulk-type SSBs.

In situ differential electrochemical mass spectrometry (DEMS) measurements were performed to further evaluate the effectiveness of the coating in suppressing outgassing reactions.<sup>[52]</sup> In recent years, it has been shown that certain coating chemistries are capable of reducing the evolution of gaseous degradation products that are detrimental to the battery operation.<sup>[41,52]</sup> The DEMS results for the different NCM85 CAMs are shown in Figure 6 and Figures S25–S28 (Supporting Information). Four different gases were detected,  $H_2$ ,  $O_2$ ,  $CO_2$ , and  $SO_2$ . Because ToF-SIMS analysis showed a decrease in  $SO_x^-$  fragments for the  $ZrO_2$ -NCM85 cell, both the  $O_2$  evolution and the  $SO_2$  evolution were of great importance here. SSB cells using the bare NCM85 and  $ZrO_2$ -NCM85 CAMs (see Figure S27, Supporting Information,

for C-NCM85) were cycled for 2 cycles and the respective gas-gassing (see Figures S25 and S27, Supporting Information, for  $H_2$  and  $CO_2$ ) was observed at increasing onset voltages. In SSBs with Ni-rich NCM CAMs,  $O_2$  (potentially reactive singlet oxygen,  $^1O_2$ ) release is typically observed at a state of charge (SOC)  $\geq 80\%$ . The origin of  $O_2$  evolution during cycling stems from the destabilization of the layered lattice at high voltages (e.g.,  $>4.2$  V vs  $Li^+/Li$  for NCM811).<sup>[53,54]</sup> Unfortunately, not all cells in this study were able to achieve the SOC requirement of  $\geq 80\%$ . While the bare NCM85 cell showed a 75% SOC (206 mAh  $g_{NCM85}^{-1}$ ), the  $ZrO_2$ -NCM85 cell achieved an SOC of 84% (229 mAh  $g_{NCM85}^{-1}$ ). Nevertheless, it has been shown that  $O_2$  evolution may occur even below 80% because of inhomogeneities throughout the cathode composite.<sup>[55–57]</sup> A case in point, the mass signal ( $m/z = 32$ ) of the cell containing the bare NCM85 showed a sharp peak (Figure 6a) upon reaching a voltage of  $\approx 4.2$  V versus  $Li^+/Li$ . By contrast, the  $ZrO_2$ -NCM85 (Figure 6b) did not reveal any distinct peaks corresponding to  $O_2$  release. Similarly,  $O_2$  evolution was not apparent for the cell using the C-NCM85 (Figure S27, Supporting Information). Recently, Guo et al. reported about oleic acid-induced surface engineering, leading to the formation of a protective spinel type  $Li_4Mn_5O_{12}$  layer on Li-rich layered oxide CAMs. According to the authors, the as-formed heterostructure is capable of stabilizing the surface, thereby suppressing  $O_2$  release and preventing related phase transformations and side reactions from occurring.<sup>[58]</sup> Because the coating method employed in this

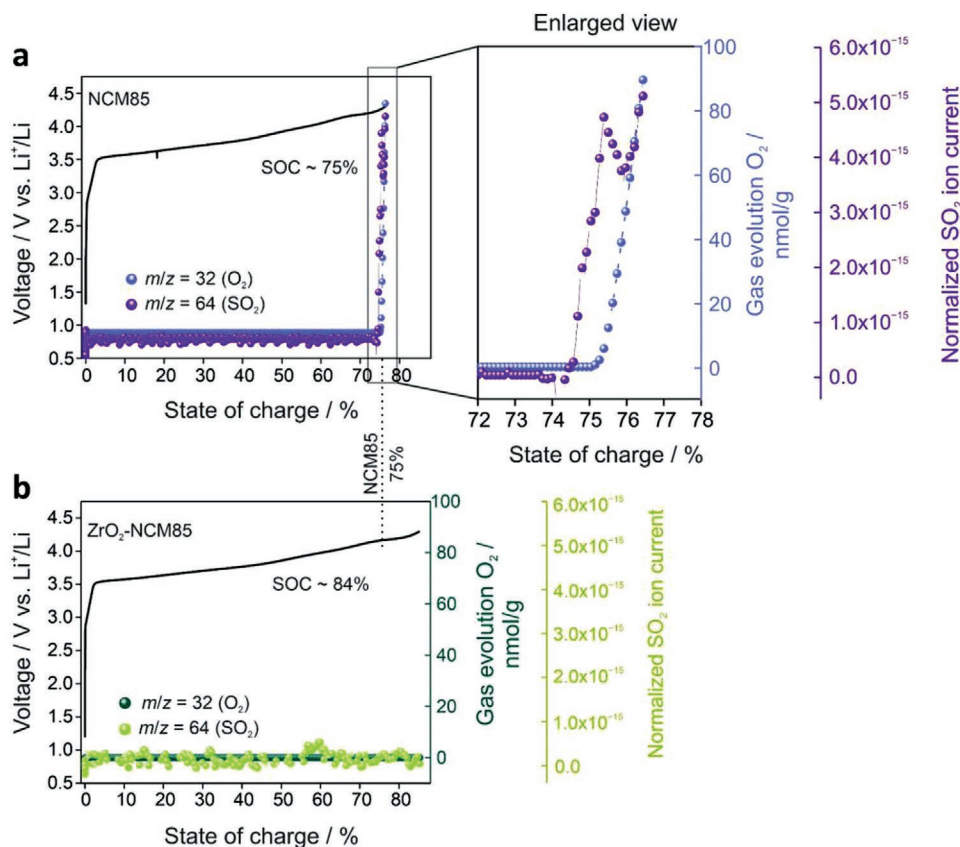


**Figure 6.** In situ DEMS analysis of SSB cells using the a) bare NCM85 and b)  $ZrO_2$ -NCM85 during the first charge cycle at a rate of 0.05 C and 45 °C. The voltage and corresponding cumulative gas evolution of  $O_2$  and normalized ion current for  $SO_2$  are plotted versus the SOC.

work comprised the use of oleic acid as a stabilizing agent for the  $\text{ZrO}_2$  NPs, surface reconstruction may play a role here as well. In fact, EELS mapping of the C-NCM85 indicated Mn enrichment at the particle surface (Figure S29, Supporting Information), but this needs further study. An additional difference between the bare and coated NCM85 CAMs was the lack of  $\text{SO}_2$  evolution for the latter samples.  $\text{SO}_2$  release is characteristic of SSBs with thiophosphate SEs, and a mass signal ( $m/z = 64$ ) is normally detected together with the  $\text{O}_2$  signal. The formation of  $\text{SO}_2$  has been reported to be a result of the reaction between SE and reactive oxygen released from both the NCM lattice at high SOC and electrochemical decomposition of residual surface carbonates.<sup>[56,59]</sup> For the bare NCM85, the observed onset of  $\text{SO}_2$  evolution coincides with the  $\text{O}_2$  and  $\text{CO}_2$  signals. On the other hand, no apparent  $\text{SO}_2$  signal was observed for the  $\text{ZrO}_2$ -NCM85 CAM, and neither for the C-NCM85. This observation indicates that the coating indirectly suppresses the  $\text{O}_2$  evolution, and in doing so, suppresses interfacial side reactions to some extent, as evidenced by the lack of gaseous degradation products ( $\text{SO}_2$ ). Since reported  $\text{SO}_x^-$  peaks in XPS studies of sulfide-based battery systems are due to the reaction between SE and CAM,<sup>[60]</sup> the suppressed  $\text{SO}_x^-$  signals for the  $\text{ZrO}_2$ -NCM85 agree well with the lack of  $\text{SO}_2$  evolution.

In conclusion, in situ gas analysis of the different SSBs showed a lack of both  $\text{O}_2$  evolution and  $\text{SO}_2$  evolution for the coated CAMs at high SOC. Considering the above data from

ToF-SIMS and XPS, this result provides profound evidence of decreased oxidation of the argyrodite SE, which is beneficial to the long-term cycling performance and safety of the cells.

To demonstrate that the improvement in cycling performance achieved by applying the NP coating concept to the NCM85 CAM is not limited to an SSB environment, the electrochemical properties of the  $\text{ZrO}_2$ -NCM85 were also probed in liquid electrolyte-based LIB cells using the bare NCM85 as a reference (see Figure S30, Supporting Information, for a comparison of LIB and SSB cells).<sup>[61]</sup> Specifically, both the  $\text{ZrO}_2$ -NCM85 and bare NCM85 cathodes with high areal loadings of  $(11.3 \pm 0.3) \text{ mg}_{\text{NCM85}} \text{ cm}^{-2}$  were cycled at 0.2 C/0.2 C rate and 45 °C in coin cells in a voltage range of 2.9–4.3 V versus  $\text{Li}^+/\text{Li}$ . The initial voltage profiles (Figure 7a) and corresponding differential capacity curves (Figure S31, Supporting Information) revealed that the CAMs show a similar electrochemical behavior ( $q_{\text{dis}} \approx 206/213 \text{ mAh g}_{\text{NCM85}}^{-1}$  and Coulombic efficiencies of 93/94%). However, the  $\text{ZrO}_2$ -NCM85 exhibited a much better stability over 100 cycles, with a capacity retention of 83% (Figure 7b). By contrast, the bare NCM85 cell showed rapid fading to 113  $\text{mAh g}_{\text{NCM85}}^{-1}$ , corresponding to only 53% retention after 100 cycles.

Finally, different NP chemistries were examined in some detail to highlight the versatility of the coating strategy. As an example, 0.82 wt%  $\text{HfO}_2$  NPs ( $\approx 6 \text{ nm}$  particle size) were applied as surface coating to the NCM85 secondary particles (details in the Experimental Section). SEM imaging and EDS

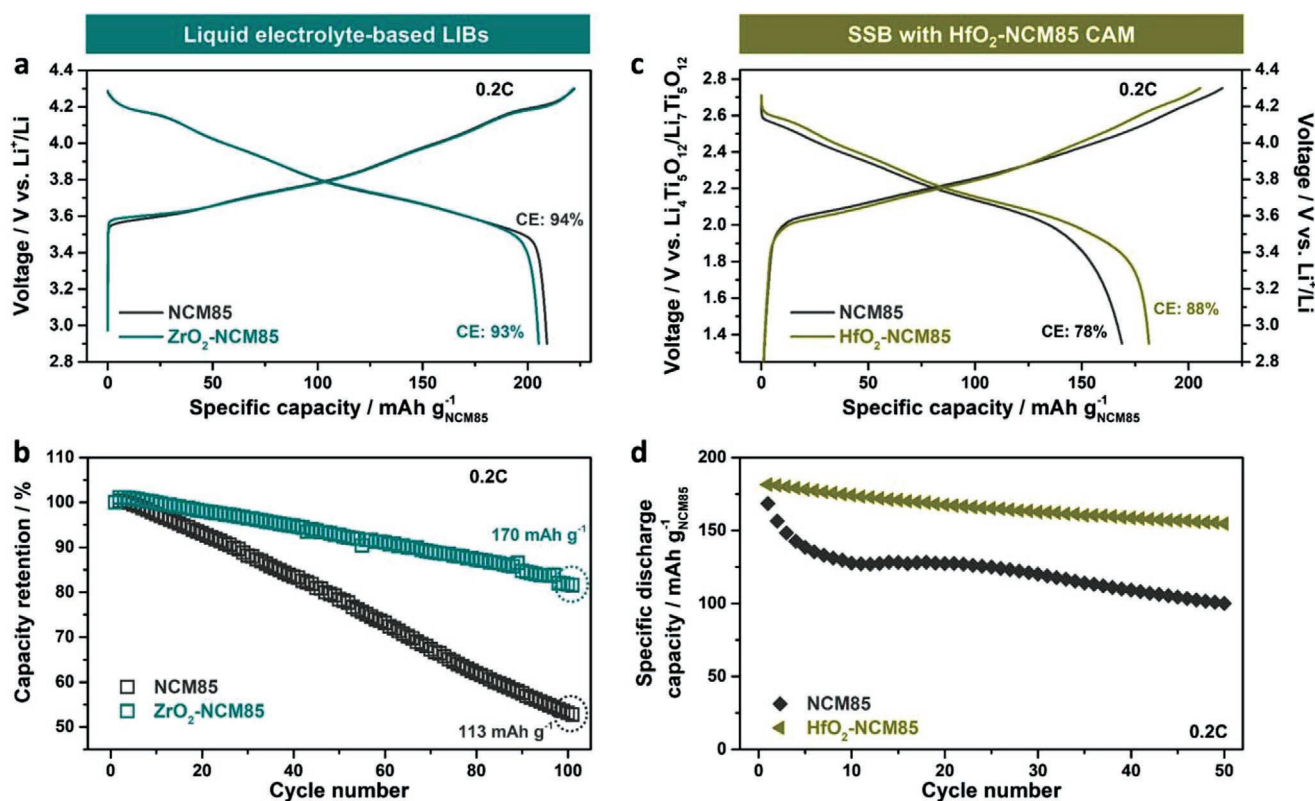


**Figure 7.** a,b) Cycling performance of  $\text{ZrO}_2$ -NCM85/Li and bare NCM85/Li cells with a liquid carbonate electrolyte at a rate of 0.2 C and 45 °C. c,d) Cycling performance of bare NCM85- and  $\text{HfO}_2$ -NCM85-based SSB cells at a rate of 0.2 C and 45 °C. (a,c) Initial voltage profiles. (b) Capacity retention and (d) specific discharge capacity versus the cycle number.

analysis confirmed the successful coating (Figure S32, Supporting Information). The as-prepared CAM (HfO<sub>2</sub>-NCM85) was tested in pelletized SSBs under the same conditions as above. The positive effect of the protective coating on the cell performance is evident from the data shown in Figure 7c,d. As can be seen from Figure 7c, the HfO<sub>2</sub>-NCM85 CAM delivered a larger first-cycle specific discharge capacity (181 vs 168 mAh g<sub>NCM85</sub><sup>-1</sup>) and showed an improved Coulombic efficiency (88 vs 78%) over the bare NCM85. More importantly, the cell using the HfO<sub>2</sub>-NCM85 CAM showed superior cyclability (Figure 7d) and was still capable of delivering a specific capacity of 156 mAh g<sub>NCM85</sub><sup>-1</sup> after 50 cycles. Overall, these results suggest that the NP strategy offers the potential to develop a variety of coating materials with clear benefits to the electrochemical performance in both SSBs and conventional liquid electrolyte-based LIBs.

### 3. Conclusions

This work has demonstrated the effectiveness of a new coating strategy based on preformed (nonagglomerated) NPs in solution in improving the cycling performance and stability of a layered Ni-rich CAM in bulk-type SSB cells. A nanoscale coating with a robust structure, consisting of a ZrO<sub>2</sub> NP monolayer and a carbonaceous layer, was successfully constructed on the surface of NCM85 secondary particles. Importantly, the as-fabricated coating not only showed a high CAM surface coverage, but also had a uniform morphology with a desirable thickness. Consequently, substantial improvements to the interfacial stability in the cathode composite were achieved, thanks to the suppression of side reactions, as confirmed by EIS, XPS, and ToF-SIMS. In addition, DEMS measurements revealed that the coating positively affects the outgassing behavior. Overall, Li<sub>6</sub>PS<sub>5</sub>Cl-based SSB cells using the surface-protected NCM85 CAM exhibited superior Li-storage performance at 45 °C.

The data presented herein are promising, and we believe that this relatively simple and likely scalable coating approach will be of great interest to the battery community. Apart from SSBs, the coating strategy also holds promise for liquid electrolyte-based LIBs and can be readily extended to other NP chemistries, showing its versatility and effectiveness. Future experiments, exploring Li-based (ternary) oxide NPs as coating materials and/or applying them to single-crystalline CAMs may foster the development of high-performance electrode materials for various battery applications.<sup>[62]</sup>

### 4. Experimental Section

**Preparation of ZrO<sub>2</sub> NP Dispersion:** ZrO<sub>2</sub> NPs were produced through a microwave-assisted solvothermal approach utilizing a Discover SP microwave (CEM GmbH), as reported previously.<sup>[30]</sup> All precursor preparation steps were performed in an Ar glovebox. The Zr precursor (zirconium(IV) isopropoxide isopropanol complex, 230 mg) was added to a microwave vial (10 mL inner volume) together with 4.5 mL benzyl alcohol, which was then sealed carefully using a Teflon cap. After 10 min of stirring at room temperature, the as-prepared solution was executed to a two-step microwave procedure: i) stirring at 60 °C for 5 min and ii) heating at 280 °C for 5 h. During the synthesis, the zirconium precursor solution transformed into a mixture consisting of a milky precipitate and

an organic supernatant. The precipitate was separated by centrifugation and washed four times with diethyl ether. For XRD investigation, the resulting product was dried at 60 °C overnight. For the preparation of a stable and well-dispersed ZrO<sub>2</sub> NP solution, the white powder was not dried after washing, but chloroform containing oleic acid (30 mg in 10 mL) was added immediately after the decantation. Upon stirring overnight, a transparent dispersion (see photographs in Figure S3, Supporting Information) was formed, having a solid content of ≈70 mg mL<sup>-1</sup>.

**Preparation of ZrO<sub>2</sub>-NCM85 and C-NCM85:** The NCM85 powder was regenerated first to remove any surface impurities. Specifically, the CAM (15 g) was heated at 750 °C (5 °C min<sup>-1</sup> heating ramp) for 3 h under O<sub>2</sub> flow in an alumina crucible. Then, the bare NCM85 powder (2 g) was mixed with a certain volume of the ZrO<sub>2</sub> NP dispersion in a beaker before adding chloroform to achieve a volume of 20 mL in total. After sonication for 30 min, the as-prepared suspension was dried at 60 °C under mild stirring, and the remaining powder was vacuum-dried at room temperature overnight. Subsequently, the modified CAM was transferred to a tube furnace and heated at 400 °C (5 °C min<sup>-1</sup> heating ramp) for 2 h under O<sub>2</sub> flow. Finally, the resulting material, ZrO<sub>2</sub>-NCM85, was collected. For C-NCM85, the same procedure was followed, but without adding ZrO<sub>2</sub> NPs in the chloroform-based solution (it just contained the oleic acid).

**Preparation of HfO<sub>2</sub>-NCM85:** For the synthesis of HfO<sub>2</sub> NPs, the work followed an established solvothermal process with some modifications.<sup>[63]</sup> 200 mg hafnium chloride was dissolved into 20 mL benzyl alcohol under vigorous stirring. After 15 min, a colorless and clear solution was formed for further use. The reaction mixture was added to a Teflon cup (45 mL inner volume) in a steel autoclave. The solvothermal reaction was performed in a furnace at 250 °C for 3 d. The NPs were recovered by precipitation using diethyl ether, followed by washing with both ethanol and diethyl ether. Finally, the HfO<sub>2</sub> NPs were redispersed in 5.5 mL chloroform for further modification. Postfunctionalization included adding oleic acid and oleylamine to the suspension under stirring until a transparent dispersion was achieved.<sup>[32]</sup> Coating of the NCM85 followed the same procedure as for the ZrO<sub>2</sub>-NCM85 CAM.

**Basic Characterization:** Powder XRD data were collected using a STOE Stadi-P diffractometer with a Mo anode ( $\lambda = 0.70926 \text{ \AA}$ ) and a DECTRIS MYTHEN 1K strip detector in Debye-Scherrer geometry. The instrumental contribution to the reflection broadening was determined by measuring a NIST 640f Si standard reference material. Rietveld refinement was performed using GSAS-II.<sup>[64]</sup> The scale factor, zero shift, and size/strain broadening parameters were allowed to vary. A fixed background was fitted to the data using a Chebyshev polynomial function with 11 terms. In the structural model, the unit cell parameters, oxygen z-coordinate, and atomic displacement parameters (isotropic) for each site were refined. Atoms occupying the same site were constrained to have the same atomic parameters, and site occupancy factors were constrained such that each site remained fully occupied. The site occupancy factor of Ni in the Li layer was refined to verify the off-stoichiometry. SEM imaging was done on a LEO-1530 microscope (Carl Zeiss AG) with a field emission source. TEM was performed both on a Titan 80–300 image-corrected microscope (FEI) and on a Themis Z (ThermoFisher Scientific) double-corrected transmission electron microscope equipped with an EDAX SuperX EDS detector. The acceleration voltage used for both microscopes was 300 kV. EELS data were acquired with an energy resolution of ≈1 eV, estimated from the FWHM of the zero-loss peak by a Gatan image filter with K3 camera (Gatan Inc.). Samples for TEM were prepared by the lift-out technique using a Ga FIB on a STRATA dual-beam system (ThermoFisher Scientific). Prior to the ion milling, the ZrO<sub>2</sub>-NCM85 CAM surface was protected by a carbon layer. Carbon was chosen for coating to exclude possible redeposition of Pt during the final milling steps. By contrast, Pt was chosen as a protective coating for the C-NCM85 CAM. The samples were milled at 30 kV, followed by final polishing at 2 kV to reduce the surface layer damage. Scanning TEM images were collected using an HAADF detector. An ALPHA FT-IR spectrometer (Bruker) was used to collect ATR-IR spectra. The instrument was equipped with a Ge crystal and situated in an Ar glovebox. The ZrO<sub>2</sub> content after coating was determined by ICP-OES using both a PerkinElmer Optima 4300 DV and a Thermo Scientific iCAP 7600.

**XPS Analysis:** XPS measurements were performed using a PHI5000 Versa Probe II system (Physical Electronics). The samples were prepared in an Ar glovebox. Insulating adhesive tape was used to attach the composite cathodes to the sample holder. The samples were transferred to the instrument under inert atmosphere using a transfer vessel from PREVAC. A dual-beam charge neutralization (low-energy electron beam combined with an ion beam) was used during the analysis. Depth profiling (alternating sputter mode) was carried out to minimize the detrimental effect of the current collector and to monitor the surface cleaning process, analogous to previous works.<sup>[45,48]</sup> Monochromatic Al-K $\alpha$  radiation ( $\lambda = 1486.6$  eV) was used for analysis (200  $\mu\text{m}$  spot diameter). The power of the X-ray source was 50 W with a voltage of 17 kV. For acquiring detailed spectra, the pass energy of the analyzer was set to 23.50 eV. A sputter gun (Ar<sup>+</sup> ions) was used for material abrasion (2  $\times$  2 mm<sup>2</sup> raster size). The acceleration voltage was set to 0.5 kV and the sputter current was  $\approx 0.5$   $\mu\text{A}$ . Data evaluation was performed with the software CasaXPS (version 2.3.22, Casa Software). The energy-calibration procedure was done as described in previous studies.<sup>[45,48,65,66]</sup> The XPS data collected from a Li<sub>6</sub>PS<sub>5</sub>Cl reference were calibrated first to the signal of adventitious carbon at 284.8 eV. Subsequently, the position of the Cl 2p signal was determined, and the spectra of all composite cathodes were then calibrated in relation to the Cl 2p component at 198.8 eV. The suitability of this energy-calibration procedure was double-checked with the main components of the SE. For signal fitting, Shirley backgrounds, GL(30) line shapes, and common fitting restrictions, such as theoretical signal area ratios, FWHM constraints, and reported values for the spin-orbit splitting, were used.<sup>[67]</sup>

**ToF-SIMS Analysis:** ToF-SIMS measurements were performed on a TOF.SIMS 5–100 system (IONTOF). The samples were prepared in an Ar glovebox. Insulating adhesive tape was used to attach the composite cathodes to the sample holder. The samples were transferred to the instrument under inert atmosphere using the transfer system Leica EM VCT500 (Leica Microsystems). All measurements were performed in negative ion mode using Bi<sub>3</sub><sup>+</sup> (25 keV) as primary ions. Low-energy electrons were introduced to the surface for charge compensation. The cycle time was 60  $\mu\text{s}$  in all cases. Surface analysis was performed in spectrometry mode (bunched mode) to enable high signal intensities and high mass resolution. The analysis area was 150  $\times$  150  $\mu\text{m}^2$  and rasterized with 256  $\times$  256 pixels (random mode). Every patch was analyzed with 1 frame and 1 shot per pixel and frame. The measurement was stopped after a primary ion dose of 10<sup>12</sup> ions cm<sup>-2</sup> was reached (static conditions). The primary ion current was  $\approx 0.7$  pA for all measurements. At least 14 mass spectra per sample were acquired in different areas on the surface of the composite cathodes to minimize local compositional differences and ensure reproducibility. Depth profiling was also done in spectrometry mode. The analysis area was 300  $\times$  300  $\mu\text{m}^2$  and rasterized with 512  $\times$  512 pixels (sawtooth mode). Every patch was analyzed with 3 frames and 1 shot per pixel and frame. The primary ion current was  $\approx 0.5$  pA. For material abrasion, a dual-source column with Cs<sup>+</sup> (500 eV) as sputter species was used (700  $\times$  700  $\mu\text{m}^2$  raster size). Depth profiling was performed in non-interlaced mode with 4 sputter frames, followed by a pause of 1 s. The sputter current was  $\approx 19$  nA. At least 3 depth profiles per sample were measured. To minimize the detrimental influence of the current collector, a z-region-of-interest (ROI) was evaluated. Accordingly, the scans 4–12 were taken into account for all samples, excluding the direct surface region. ToF-SIMS measurements were performed on 45° FIB crater sidewalls. The craters (120  $\times$  80  $\mu\text{m}^2$  crater size) were milled into the composite cathodes using the FIB option attached to the instrument. A 700  $\mu\text{m}$  aperture was used and the dwell time set to 200 ms per pixel (150  $\times$  150  $\mu\text{m}^2$ , 512  $\times$  512 pixels). The FIB current was  $\approx 23$  nA (100% duty cycle). The crater sidewall was analyzed by operating the instrument in fast imaging mode. The primary ion current was between 0.1 and 0.2 pA. An ROI was defined to measure only on the crater sidewall (125  $\times$  125  $\mu\text{m}^2$ ). Prior to analysis, the FIB damage layer on the surface was removed by a cleaning procedure described elsewhere.<sup>[45]</sup> The subsequent analysis (50 scans) was performed with a raster size of 1024  $\times$  1024 pixels at 1 shot per pixel and 1 frame (random mode). This led to a theoretical maximum

lateral resolution of 122 nm (under ideal conditions/lower limit). Data evaluation was done using the software SurfaceLab 7.0 (IONTOF). All mass spectra and secondary ion images were normalized to the total ion signal.

**In Situ Gas Analysis:** The SSBs used for in situ DEMS measurements were assembled in a customized cell, which has been described in detail in previous studies.<sup>[55,56]</sup> The cell components were similar to those assembled for electrochemical testing (below), except that In foil was used as anode. Cycling was performed at 45 °C and 0.05 C rate in a voltage range of 2.3–3.7 V versus In/InLi ( $\approx 2.9$ –4.3 V vs Li<sup>+</sup>/Li) using a VMP3 multichannel potentiostat (Biologic). All cells underwent a 10 h open-circuit voltage (OCV) period prior to cycling to achieve a stable baseline for the mass spectrometer. The flow of He carrier gas (2.5 mL min<sup>-1</sup>) was controlled by a mass flow controller (Bronkhorst; F-201CV-020-RAD-33-Z). For DEMS analysis, a mass spectrometer from Pfeiffer Vacuum GmbH (OmniStar GSD 320 O2) was used. After each measurement, a calibration gas with known quantity of H<sub>2</sub>, CO<sub>2</sub>, and O<sub>2</sub> (ppm) was introduced to the system to convert the measured ion currents into mol g<sup>-1</sup> values.

**Electrode Preparation:** The cathode composites for testing in SSB cells were prepared as reported elsewhere.<sup>[18,24]</sup> In brief, the CAM was mixed with the argyrodite Li<sub>6</sub>PS<sub>5</sub>Cl SE (NEI Corp.) and Super C65 carbon black additive (Timcal) in a 69.3:29.7:1 weight ratio for 0.5 h at 140 rpm under Ar atmosphere using a planetary ball-mill with 1 cm diameter zirconia balls. The preparation of the anode composite was similar, but the weight ratio of carbon-coated LTO (NEI Corp.), Super C65, and Li<sub>6</sub>PS<sub>5</sub>Cl was set to 30:10:60. The SE-Super C65 composite used in the CV experiment was prepared by manually grinding both materials for 0.5 h using a mortar and pestle. For the LIB cells, the *N*-methyl-2-pyrrolidone cathode slurry contained 94 wt% CAM, 3 wt% Super C65, and 3 wt% polyvinylidene fluoride binder. The cathode sheet was prepared by slurry casting onto Al foil, followed by drying at 120 °C in a vacuum and calendaring at 15 N mm<sup>-1</sup>. Finally, 13 mm diameter (circular) electrodes with an areal loading of  $\approx 11.3$  mg<sub>NCM85</sub> cm<sup>-2</sup> were punched out.

**Cell Assembly and Electrochemical Measurements:** All SSB and LIB cells were assembled in an Ar glovebox. For the SSBs, the electrochemical performance was probed using a custom-built cell setup (see Figure S33, Supporting Information) with two stainless steel dies and a PEEK ring. Specifically, 100 mg Li<sub>6</sub>PS<sub>5</sub>Cl SE was pressed at 62.5 MPa. Next, 12–13 mg cathode composite and the anode composite were separately filled at opposite ends and compressed at 440 MPa. For investigating the electrochemical stability window of the Li<sub>6</sub>PS<sub>5</sub>Cl SE, 12–13 mg SE-Super C65 composite was attached to the SE pellet and pressed at 62.5 MPa, followed by In foil onto the other side. The galvanostatic (dis-)charge and rate capability measurements were performed at 81 MPa and 45 °C and at C-rates ranging from 0.1 C to 6.0 C (1.0 C = 190 mA g<sub>NCM85</sub><sup>-1</sup>). Testing of the SSB cells was done in a voltage range of 1.35–2.75 V versus Li<sub>4</sub>Ti<sub>5</sub>O<sub>12</sub>/Li<sub>7</sub>Ti<sub>5</sub>O<sub>12</sub> ( $\approx 2.9$ –4.3 V vs Li<sup>+</sup>/Li) after a 1 h OCV period using a MACCOR battery cycler. The electrochemical properties of LIBs were probed in 2032 coin cells with a Li-metal counter electrode (Albemarle Germany GmbH). Glass fiber (GF/D, Whatman) soaked with 100  $\mu\text{L}$  of LP57 (1 M LiPF<sub>6</sub> in 3:7 by weight ethylene carbonate and ethyl methyl carbonate, BASF SE) was used as separator. The galvanostatic cycling tests were performed at 0.2 C rate and 45 °C in a voltage range of 2.9–4.3 V versus Li<sup>+</sup>/Li using a MACCOR battery cycler. GITT measurements were performed after the first cycle with a constant current of 0.05 C for 0.5 h and a relaxation step of 4 h. EIS was measured both at 25 and 45 °C using an SP-300 potentiostat (BioLogic) in a frequency range between 100 mHz and 7 MHz (7 mV voltage amplitude). CV measurements were conducted on the same instrument at 45 °C in a voltage range of 1.35–2.75 V versus Li<sub>4</sub>Ti<sub>5</sub>O<sub>12</sub>/Li<sub>7</sub>Ti<sub>5</sub>O<sub>12</sub> (0–5.0 or 0–3.2 V vs In/InLi for probing the electrochemical stability window of the Li<sub>6</sub>PS<sub>5</sub>Cl SE).

## Supporting Information

Supporting Information is available from the Wiley Online Library or from the author.

## Acknowledgements

This study was supported by BASF SE. The authors acknowledge the support from the Karlsruhe Nano Micro Facility (KNMF, www.knmf.kit.edu), a Helmholtz research infrastructure at Karlsruhe Institute of Technology (KIT, www.kit.edu). The authors would like to thank Dr. Thomas Bergfeldt for ICP-OES measurements. Y.T. acknowledges the financial support from the German Research Foundation (DFG) under Project ID 390874152 (POLiS Cluster of Excellence).

Open access funding enabled and organized by Projekt DEAL.

## Conflict of Interest

The authors declare no conflict of interest.

## Data Availability Statement

The data that support the findings of this study are available from the corresponding author upon reasonable request.

## Keywords

all-solid-state battery, interfacial stability, layered Ni-rich oxide cathode, protective coating, side reactions

Received: November 19, 2021

Revised: January 27, 2022

Published online:

- [1] Y.-G. Lee, S. Fujiki, C. Jung, N. Suzuki, N. Yashiro, R. Omoda, D.-S. Ko, T. Shiratsuchi, T. Sugimoto, S. Ryu, J. H. Ku, T. Watanabe, Y. Park, Y. Aihara, D. Im, I. T. Han, *Nat. Energy* **2020**, *5*, 299.
- [2] A. Banerjee, X. Wang, C. Fang, E. A. Wu, Y. S. Meng, *Chem. Rev.* **2020**, *120*, 6878.
- [3] J. Janek, W. G. Zeier, *Nat. Energy* **2016**, *1*, 16141.
- [4] R. Chen, Q. Li, X. Yu, L. Chen, H. Li, *Chem. Rev.* **2020**, *120*, 6820.
- [5] L. Zhou, C. Y. Kwok, A. Shyamsunder, Q. Zhang, X. Wu, L. F. Nazar, *Energy Environ. Sci.* **2020**, *13*, 2056.
- [6] K. Xu, *Chem. Rev.* **2014**, *114*, 11503.
- [7] D. H. S. Tan, A. Banerjee, Z. Chen, Y. S. Meng, *Nat. Nanotechnol.* **2020**, *15*, 170.
- [8] Y. Ma, J. H. Teo, D. Kitsche, T. Diemant, F. Strauss, Y. Ma, D. Goonetilleke, J. Janek, M. Bianchini, T. Brezesinski, *ACS Energy Lett.* **2021**, *6*, 3020.
- [9] S. P. Culver, R. Koerver, W. G. Zeier, J. Janek, *Adv. Energy Mater.* **2019**, *9*, 1900626.
- [10] P. Minnmann, L. Quillman, S. Burkhardt, F. H. Richter, J. Janek, *J. Electrochem. Soc.* **2021**, *168*, 040537.
- [11] Z. Zhang, Y. Shao, B. Lotsch, Y.-S. Hu, H. Li, J. Janek, L. F. Nazar, C.-W. Nan, J. Maier, M. Armand, L. Chen, *Energy Environ. Sci.* **2018**, *11*, 1945.
- [12] S. Randau, D. A. Weber, O. Kötz, R. Koerver, P. Braun, A. Weber, E. Ivers-Tiffée, T. Adermann, J. Kulisch, W. G. Zeier, F. H. Richter, J. Janek, *Nat. Energy* **2020**, *5*, 259.
- [13] J. Zhang, C. Zheng, L. Li, Y. Xia, H. Huang, Y. Gan, C. Liang, X. He, X. Tao, W. Zhang, *Adv. Energy Mater.* **2020**, *10*, 1903311.
- [14] N. Nitta, F. Wu, J. T. Lee, G. Yushin, *Mater. Today* **2015**, *18*, 252.
- [15] M. Yoon, Y. Dong, J. Hwang, J. Sung, H. Cha, K. Ahn, Y. Huang, S. J. Kang, J. Li, J. Cho, *Nat. Energy* **2021**, *6*, 362.
- [16] Z. Chen, G.-T. Kim, D. Bresser, T. Diemant, J. Asenbauer, S. Jeong, M. Copley, R. J. Behm, J. Lin, Z. Shen, S. Passerini, *Adv. Energy Mater.* **2018**, *8*, 1801573.
- [17] W. D. Richards, L. J. Miara, Y. Wang, J. C. Kim, G. Ceder, *Chem. Mater.* **2016**, *28*, 266.
- [18] F. Walther, F. Strauss, X. Wu, B. Mogwitz, J. Hertle, J. Sann, M. Rohnke, T. Brezesinski, J. Janek, *Chem. Mater.* **2021**, *33*, 2110.
- [19] Y. Zhu, X. He, Y. Mo, *ACS Appl. Mater. Interfaces* **2015**, *7*, 23685.
- [20] Y. Xiao, L. J. Miara, Y. Wang, G. Ceder, *Joule* **2019**, *3*, 1252.
- [21] U. Nisar, N. Muralidharan, R. Essehli, R. Amin, I. Belharouak, *Energy Storage Mater.* **2021**, *38*, 309.
- [22] B. Ahmed, C. Xia, H. N. Alshareef, *Nano Today* **2016**, *11*, 250.
- [23] B. Xiao, B. Wang, J. Liu, K. Kaliyappan, Q. Sun, Y. Liu, G. Dadheech, M. P. Balogh, L. Yang, T.-K. Sham, R. Li, M. Cai, X. Sun, *Nano Energy* **2017**, *34*, 120.
- [24] D. Kitsche, Y. Tang, Y. Ma, D. Goonetilleke, J. Sann, F. Walther, M. Bianchini, J. Janek, T. Brezesinski, *ACS Appl. Energy Mater.* **2021**, *4*, 7338.
- [25] J. Cho, Y.-W. Kim, B. Kim, J.-G. Lee, B. Park, *Angew. Chem., Int. Ed.* **2003**, *42*, 1618.
- [26] Y.-S. Lee, W.-K. Shin, A. G. Kannan, S. M. Koo, D.-W. Kim, *ACS Appl. Mater. Interfaces* **2015**, *7*, 13944.
- [27] C. Geng, A. Liu, J. R. Dahn, *Chem. Mater.* **2020**, *32*, 6097.
- [28] J. Cho, Y. J. Kim, T.-J. Kim, B. Park, *Angew. Chem., Int. Ed.* **2001**, *40*, 3367.
- [29] N. Machida, J. Kashiwagi, M. Naito, T. Shigematsu, *Solid State Ion* **2012**, *225*, 354.
- [30] K. De Keukeleere, J. De Roo, P. Lommens, J. C. Martins, P. Van Der Voort, I. Van Driessche, *Inorg. Chem.* **2015**, *54*, 3469.
- [31] N. Pinna, M. Niederberger, *Angew. Chem., Int. Ed.* **2008**, *47*, 5292.
- [32] J. De Roo, F. Van den Broeck, K. De Keukeleere, J. C. Martins, I. Van Driessche, Z. Hens, *J. Am. Chem. Soc.* **2014**, *136*, 9650.
- [33] G. Garnweitner, L. M. Goldenberg, O. V. Sakhno, M. Antonietti, M. Niederberger, J. Stumpe, *Small* **2007**, *3*, 1626.
- [34] Y. Jun, J. Choi, J. Cheon, *Angew. Chem., Int. Ed.* **2006**, *45*, 3414.
- [35] L. Armelao, E. Tondello, L. Bigliani, G. Bottaro, *Surf. Sci. Spectra* **2001**, *8*, 268.
- [36] L. Sygellou, V. Gianneta, N. Xanthopoulos, D. Skarlatos, S. Georga, C. Krontiras, S. Ladas, S. Kennou, *Surf. Sci. Spectra* **2011**, *18*, 58.
- [37] A. C. Kozen, A. J. Pearse, C.-F. Lin, M. A. Schroeder, M. Noked, S. B. Lee, G. W. Rubloff, *J. Phys. Chem. C* **2014**, *118*, 27749.
- [38] K. Kanamura, H. Tamura, S. Shiraiishi, Z. Takehara, *J. Electrochem. Soc.* **1995**, *142*, 340.
- [39] Y. Ma, Y. Ma, G. Kim, T. Diemant, R. J. Behm, D. Geiger, U. Kaiser, A. Varzi, S. Passerini, *Adv. Energy Mater.* **2019**, *9*, 1902077.
- [40] T. Hatsukade, A. Schiele, P. Hartmann, T. Brezesinski, J. Janek, *ACS Appl. Mater. Interfaces* **2018**, *10*, 38892.
- [41] A.-Y. Kim, F. Strauss, T. Bartsch, J. H. Teo, T. Hatsukade, A. Mazilkin, J. Janek, P. Hartmann, T. Brezesinski, *Chem. Mater.* **2019**, *31*, 9664.
- [42] Y. Ma, Y. Ma, T. Diemant, K. Cao, U. Kaiser, R. J. Behm, A. Varzi, S. Passerini, *ChemElectroChem* **2021**, *8*, 918.
- [43] R. Koerver, I. Aygün, T. Leichtweiß, C. Dietrich, W. Zhang, J. O. Binder, P. Hartmann, W. G. Zeier, J. Janek, *Chem. Mater.* **2017**, *29*, 5574.
- [44] N. Ohta, K. Takada, L. Zhang, R. Ma, M. Osada, T. Sasaki, *Adv. Mater.* **2006**, *18*, 2226.
- [45] F. Walther, R. Koerver, T. Fuchs, S. Ohno, J. Sann, M. Rohnke, W. G. Zeier, J. Janek, *Chem. Mater.* **2019**, *31*, 3745.
- [46] J. H. Teo, F. Strauss, F. Walther, Y. Ma, S. Payandeh, T. Scherer, M. Bianchini, J. Janek, T. Brezesinski, *Mater. Futures* **2022**, *1*, 015102.
- [47] B. Wang, J. Liu, Q. Sun, R. Li, T.-K. Sham, X. Sun, *Nanotechnology* **2014**, *25*, 504007.
- [48] F. Walther, S. Randau, Y. Schneider, J. Sann, M. Rohnke, F. H. Richter, W. G. Zeier, J. Janek, *Chem. Mater.* **2020**, *32*, 6123.
- [49] S. Randau, F. Walther, A. Neumann, Y. Schneider, R. S. Negi, B. Mogwitz, J. Sann, K. Becker-Steinberger, T. Danner, S. Hein, A. Latz, F. H. Richter, J. Janek, *Chem. Mater.* **2021**, *33*, 1380.
- [50] H. Visbal, Y. Aihara, S. Ito, T. Watanabe, Y. Park, S. Doo, *J. Power Sources* **2016**, *314*, 85.

- [51] R. Koerver, F. Walther, I. Aygün, J. Sann, C. Dietrich, W. G. Zeier, J. Janek, *J. Mater. Chem. A* **2017**, *5*, 22750.
- [52] F. Strauss, D. Kitsche, Y. Ma, J. H. Teo, D. Goonetilleke, J. Janek, M. Bianchini, T. Brezesinski, *Adv. Energy Sustainability Res.* **2021**, *2*, 2100004.
- [53] R. Jung, M. Metzger, F. Maglia, C. Stinner, H. A. Gasteiger, *J. Electrochem. Soc.* **2017**, *164*, A1361.
- [54] R. Jung, P. Strobl, F. Maglia, C. Stinner, H. A. Gasteiger, *J. Electrochem. Soc.* **2018**, *165*, A2869.
- [55] T. Bartsch, F. Strauss, T. Hatsukade, A. Schiele, A.-Y. Kim, P. Hartmann, J. Janek, T. Brezesinski, *ACS Energy Lett.* **2018**, *3*, 2539.
- [56] F. Strauss, J. H. Teo, A. Schiele, T. Bartsch, T. Hatsukade, P. Hartmann, J. Janek, T. Brezesinski, *ACS Appl. Mater. Interfaces* **2020**, *12*, 20462.
- [57] J. H. Teo, F. Strauss, Đ. Tripković, S. Schweidler, Y. Ma, M. Bianchini, J. Janek, T. Brezesinski, *Cell Rep. Phys. Sci.* **2021**, *2*, 100465.
- [58] W. Guo, C. Zhang, Y. Zhang, L. Lin, W. He, Q. Xie, B. Sa, L. Wang, D. Peng, *Adv. Mater.* **2021**, *33*, 2103173.
- [59] N. Mahne, S. E. Renfrew, B. D. McCloskey, S. A. Freunberger, *Angew. Chem., Int. Ed.* **2018**, *57*, 5529.
- [60] J. Auvergniot, A. Cassel, D. Foix, V. Viallet, V. Seznec, R. Dedryvère, *Solid State Ion* **2017**, *300*, 78.
- [61] R. Ruess, S. Schweidler, H. Hemmelmann, G. Conforto, A. Bielefeld, D. A. Weber, J. Sann, M. T. Elm, J. Janek, *J. Electrochem. Soc.* **2020**, *167*, 100532.
- [62] S. Payandeh, D. Goonetilleke, M. Bianchini, J. Janek, T. Brezesinski, *Curr. Opin. Electrochem.* **2022**, *31*, 100877.
- [63] J. Buha, D. Arčon, M. Niederberger, I. Djerdj, *Phys. Chem. Chem. Phys.* **2010**, *12*, 15537.
- [64] B. H. Toby, R. B. Von Dreele, *J. Appl. Crystallogr.* **2013**, *46*, 544.
- [65] F. Lindgren, D. Rehnlund, I. Källquist, L. Nyholm, K. Edström, M. Hahlin, J. Maibach, *J. Phys. Chem. C* **2017**, *121*, 27303.
- [66] J. Maibach, F. Lindgren, H. Eriksson, K. Edström, M. Hahlin, *J. Phys. Chem. Lett.* **2016**, *7*, 1775.
- [67] J. F. Moulder, W. J. Stickle, P. E. Sobol, K. D. Bomben, *Handbook of X-Ray Photoelectron Spectroscopy: A Reference Book of Standard Spectra for Identification and Interpretation of XPS Data*, Perkin-Elmer, MN, USA **1995**.